

A UNIQUE VIEW OF AGN-DRIVEN MOLECULAR OUTFLOWS: THE DISCOVERY OF A MASSIVE GALAXY COUNTERPART TO A $Z = 2.4$ HIGH-METALLICITY DAMPED LYMAN- α ABSORBER

GWEN C. RUDIE, ANDREW B. NEWMAN,
Carnegie Observatories
813 Santa Barbara Street
Pasadena, California 91101, USA

AND

MICHAEL T. MURPHY
Centre for Astrophysics and Supercomputing
Swinburne University of Technology
Hawthorn, VIC 3122, Australia
Draft version December 3, 2024

ABSTRACT

We report the discovery of massive $\log(M/M_{\odot}) = 10.74^{+0.18}_{-0.16}$ galaxy at the same redshift as a carbon-monoxide bearing sub-damped Lyman α absorber (sub-DLA) seen in the spectrum of the QSO J1439+1117. The galaxy, J1439B, is located $4''.7$ from the QSO sightline, a projected distance of 38 physical kpc at $z = 2.4189$, and exhibits broad optical emission lines ($\sigma_{[\text{OIII}]} = 303 \pm 12 \text{ km s}^{-1}$) with ratios characteristic of excitation by an active galactic nucleus (AGN). The galaxy has a factor of ~ 10 lower star formation than is typical of star-forming galaxies of the same mass and redshift. The nearby DLA is highly enriched, suggesting its galactic counterpart must be massive if it follows the $z \sim 2$ mass-metallicity relationship. Metallic absorption associated with the DLA is spread over a velocity range $\Delta v > 1000 \text{ km s}^{-1}$, suggesting an energetic origin. We explore the possibility that a different galaxy could be responsible for the rare absorber, and conclude it is unlikely based on imaging, integral field spectroscopy, and high- z massive galaxy pair statistics. We argue that the gas seen in absorption against the QSO was likely ejected from the galaxy J1439B and therefore provides a unique observational probe of AGN feedback in the distant universe.

Subject headings: galaxies: high-redshift, active — intergalactic medium — quasars: absorption lines

1. INTRODUCTION

The formation and evolution of galaxies is inextricably tied to the flow of gas into and out of galaxies through the circumgalactic medium (CGM). Galaxies in the early universe require significant gas accretion in order to power their high rates of star formation for sizable fractions of a Hubble time (see, e.g., Erb 2008 and Finlator & Davé 2008). Gas outflows are observationally known to be prevalent among high-redshift galaxies (Pettini et al. 2001; Shapley et al. 2003; Steidel et al. 2010), and cosmological semi-analytic and hydrodynamic simulations require strong feedback in order to reproduce the observed luminosity function of galaxies (White & Frenk 1991; Cole et al. 1994; Kauffmann et al. 1999; Somerville & Primack 1999; Efstathiou 2000). At low masses, the energy and momentum injected into the gas from supernovae and stellar radiation pressure is likely sufficient to drive galaxy-scale winds (Murray et al. 2011; Hopkins et al. 2012); however, at masses above M^* , feedback from active galactic nuclei (AGN) may be needed to regulate and eventually halt star formation (Benson et al. 2003; Croton et al. 2006).

The gaseous environments of high-redshift galaxies are an excellent laboratory to explore the properties of galactic accretion and winds. Studies of statistical samples of high-redshift galaxies have begun to quantify the properties of the CGM (Rudie et al. 2012; Turner et al. 2014, 2015; Rubin et al. 2015; Lau et al. 2016); however, there is still much observational and theoretical progress

needed to understand the nuanced relationship between galaxies and their gaseous surroundings, especially in regard to feedback.

One particular class of CGM absorption is known as the damped Lyman α absorber (DLA). Covering about a third of the $2 < z < 3$ sky (Fumagalli et al. 2015), DLAs contain the majority of the neutral gas at all redshifts (Tytler 1987; O’Meara et al. 2007) and are thought to trace gas within the ISM or very near to galaxies. Compared to the rest of the intergalactic medium (IGM) and CGM which is predominantly ionized, DLAs have column densities of hydrogen large enough that the outer layers absorb the incident hydrogen-ionizing photons leaving the majority of the gas within the structure neutral. For historical reasons, DLAs are usually defined as those clouds with $\log(N_{\text{HI}}) > 20.3$, although structures with somewhat lower column densities are still self-shielding (see Wolfe et al. 2005 for a review).

DLAs, like galaxies, have a wide variety of physical properties which likely reflects the diversity of their origins. The majority of DLAs are metal poor (Pettini et al. 1997; Rafelski et al. 2012; Jorgenson et al. 2013), have small physical sizes (Monier et al. 2009; Cooke et al. 2010), and are kinematically cold (Prochaska & Wolfe 1997; Neeleman et al. 2013). Although some authors have suggested they could originate in the far outskirts of more massive systems (Cooke et al. 2006; Rafelski et al. 2011), both cosmological and high-resolution simulations suggest the majority of DLAs are associated with relatively low-mass galaxies (Haehnelt et al. 1998b;

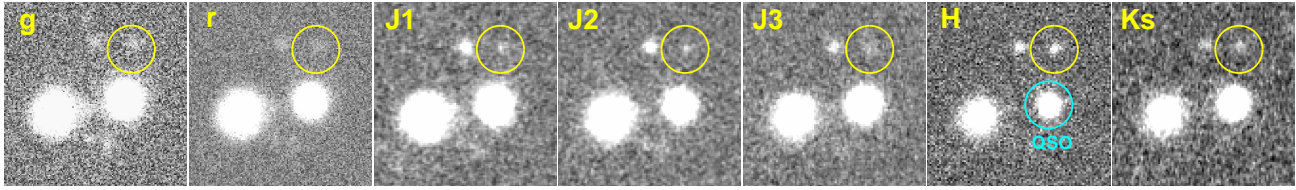


Figure 1. Optical and NIR photometry of the galaxy 4''7 from the QSO. Each panel is 15'' on a side. QSO J1439+1117 is circled in cyan in the *H*-band panel. The galaxy J1439B is circled in yellow in all panels.

Pontzen et al. 2008; Bird et al. 2015).

Tremendous effort has been focused on the identification of the galaxy counterparts of high-redshift DLAs. Large surveys of the volume surrounding QSO sight lines with DLAs have been carried out using both long slit (Fynbo et al. 2010) and integral field (Péroux et al. 2011; Bouché et al. 2012; Péroux et al. 2012) spectrographs as well as imaging and spectroscopic surveys using double DLA sight lines (Fumagalli et al. 2010). Despite these efforts, however, relatively few galaxy counterparts are known. Péroux et al. (2011), Bouché et al. (2012) and Fumagalli et al. (2015) employed systematic searches for DLA host galaxies. With relatively few detections, the authors conclude based on the detection limits of their data that the typical DLA galaxy counterpart has a star formation rate $\text{SFR} < 1 - 3 M_{\odot} \text{ yr}^{-1}$. In contrast, the detected galactic counterparts to $z > 2$ DLAs unsurprisingly represent a biased sample; the galaxies typically have significantly higher star formation rates, and on average, the metallicity of the DLAs is higher (Fynbo et al. 2010; Péroux et al. 2012; Fumagalli et al. 2015).

Fumagalli et al. (2015) recently reviewed the published results and found that only 11 $z > 1.9$, $\log(N_{\text{HI}}) > 20.3$ absorption systems were known to have galactic counterparts at the same spectroscopically identified redshift (Møller & Warren 1993; Møller et al. 2002, 2004; Weatherley et al. 2005; Fynbo et al. 2010, 2011; Bouché et al. 2012; Krogager et al. 2012; Noterdaeme et al. 2012b; Péroux et al. 2013; Bouché et al. 2013; Jorgenson & Wolfe 2014). Since 2015, at least three additional plausible host galaxies have been identified (Hartoog et al. 2015; Srianand et al. 2016). In addition to these, a handful of high- z sub-DLAs with $19.0 < \log(N_{\text{HI}}) < 20.3$ have identified nearby galaxies (c.f. Kashikawa et al. 2014; Zafar et al. 2017). Compared with either the statistical sample of DLAs from the Sloan Digital Sky Survey, which contains over 12,000 $z > 2$ DLAs (Noterdaeme et al. 2012a), or the several hundred DLAs with high-resolutions spectroscopy (see, e.g., Zafar et al. 2013; Jorgenson et al. 2013), the sample of galaxy counterparts is remarkably small. Given the current small sample, additional discoveries are critical both to our understanding of the nature of DLAs and sub-DLAs, as well as to our understanding of galaxy formation.

The sub-DLA at $z=2.41827$ towards QSO J1439+1117, hereafter DLA_{J1439}, is a unique system due to its high level of chemical enrichment and molecular gas content. It has an H I column density $N_{\text{HI}} = 20.10 \pm 0.10$, placing it just short of the classical DLA limit, and metallicity consistent with the solar value (Noterdaeme et al. 2008). DLA_{J1439} provided the first optical detection of carbon monoxide (CO) associated with a DLA

(Srianand et al. 2008). In addition to CO, other molecular species (H_2 , HD) are also detected (Srianand et al. 2008; Noterdaeme et al. 2008). Further, DLA_{J1439} has a high molecular fraction $f = 2N(\text{H}_2)/(N(\text{H I}) + 2N(\text{H}_2)) = 0.27^{+0.10}_{-0.08}$ (Srianand et al. 2008), the highest measured in any DLA to date (Liszt 2015).

Here we report the discovery of a galaxy at the same redshift $z = 2.4189$ separated from DLA_{J1439} by 4''7, or 38 physical kpc. In Section 2, we describe the imaging and spectroscopic discovery data and their analysis. Section 3 describes the properties of J1439B which indicate it likely hosts an AGN and which make it a likely galaxy counterpart to DLA_{J1439}. In Section 4, we argue that J1439B is the most likely candidate for the source of the absorber and discuss the implications for the chemical evolution of the galaxy and for AGN-driven outflows.

Throughout this paper we assume a Chabrier (2003) stellar initial mass function and a Λ -CDM cosmology with $H_0 = 70 \text{ km s}^{-1} \text{ Mpc}^{-1}$, $\Omega_m = 0.3$, and $\Omega_{\Lambda} = 0.7$. Unless otherwise specified, all distances are in physical units, all transitions are referred to by their vacuum wavelengths, and magnitudes refer to the AB system (Oke & Gunn 1983).

2. DATA

2.1. QSO Spectroscopy

High-resolution spectroscopic observations of QSO J1439+1117 were carried out using the Ultraviolet and Visual Echelle Spectrograph (UVES; Dekker et al. 2000) on the Very Large Telescope (VLT). The data from ESO program 278.A-5062(A) were obtained from the ESO Science Archive Facility. A description of the observational setup is discussed in Noterdaeme et al. (2008) and Srianand et al. (2008). All column density measurements of the absorption systems, and quantities derived from them, are taken from these papers, and the QSO data are presented in this work for visualization of the velocity distribution only.

A detailed description of the reduction procedure can be found in Murphy et al. (2007) and Bagdonaite et al. (2014). Briefly, the data were reduced using the ESO UVES pipeline. Cosmic rays were masked, and the exposures were combined using UVES_popler (Murphy 2016) which was specifically designed to optimally combine exposures reduced by the UVES pipeline. The resultant spectrum was cleaned of artifacts and continuum normalized.

2.2. Imaging Observations

Near-infrared (IR) imaging of the field surrounding QSO J1439+1117 was taken with the FourStar camera (Persson et al. 2013) on the Magellan Baade 6.5-meter telescope. The FourStar data were reduced using a custom pipeline, FourCLift, developed by D. Kelson and

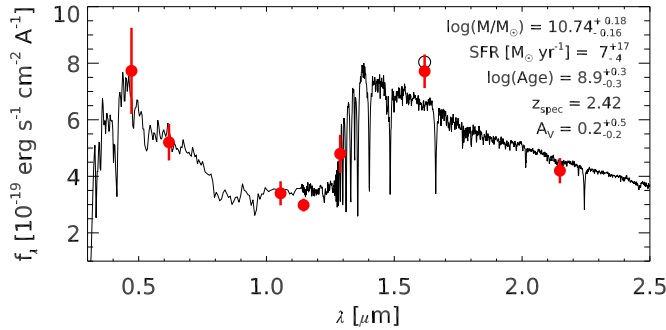


Figure 2. Aperture and foreground dust-corrected photometry of the galaxy J1439B is shown in red. The red H -band data point shows the photometry corrected for the $[\text{O III}] \lambda\lambda 5008, 4960$ line flux while the black open circle shows the photometry without this correction. In black is plotted the best-fit SED from FAST. The parameters of the best-fit model are listed in the upper right-hand corner.

described in Kelson et al. (2014). FourCLift corrects for dark current and nonlinearity before flat fielding the images. Bad pixels are masked, and the sky background is determined iteratively using a bivariate wavelet transformation of the images with detected sources masked. Time variability in each level of the wavelet transforms is determined and sky frames are computed by inverting model wavelet transforms reconstructed for the time of each science exposure. These model sky frames are subtracted, and the frames subsequently aligned and stacked, taking into account the distortion of the camera to produce rectified images. Photometric calibration of the FourCLift processed images was performed with unsaturated 2MASS stars in the field.

Optical images in Sloan g' and r' were taken with the f/2 camera of the IMACS imaging spectrometer (Dressler et al. 2011) on the Magellan Baade telescope. The data were bias and gain corrected, flat fielded, background subtracted, and combined using standard IRAF packages. The zeropoints of the images were determined using photometrically calibrated stars in the same fields from the SDSS DR7 (York et al. 2000; Abazajian et al. 2009). The optical and NIR images are shown in Figure 1. All images were aligned and then registered to the H -band image. They were then smoothed to a FWHM = $1''.2$, similar to that of the K_s band image.

2.3. Galaxy Photometry

From the NIR imaging, a galaxy of interest (henceforth J1439B) was identified $4''.7$ north of the QSO. The colors of the galaxy were measured using Source Extractor (Bertin & Arnouts 1996) in a $1''.6$ aperture centered on the H -band detection in order to minimize any contribution from the nearby QSO. A small correction to the colors for light that falls outside the $1''.6$ aperture was computed and applied by comparing the color of stars measured in $8''$ apertures to that measured in $1''.6$ apertures. Conservatively, the color errors were computed as the quadratic sum of the photometric error in the two bands and the aperture correction.

The H -band photometry of the galaxy was computed using the un-smoothed image. The Source Extractor H -band MagAuto aperture was used as the normalization and the magnitudes in the other photometric bands

Table 1
Galaxy Photometry

Band	Instrument	AB Magnitude ^a
g	IMACS	24.50 ± 0.21
r	IMACS	24.34 ± 0.13
J1	FourStar	23.65 ± 0.14
J2	FourStar	23.61 ± 0.08
J3	FourStar	22.84 ± 0.15
H	FourStar	21.78 ± 0.07
H_{corr}^b	FourStar	21.83 ± 0.08
K_s	FourStar	21.87 ± 0.12

^a Aperture and foreground dust-corrected magnitudes and errors

^b The H -band magnitude corrected for the $[\text{O III}] \lambda\lambda 5008$ and $\lambda 4960$ emission as determined from the FIRE observations.

were computed by adding the H -band magnitude to the aperture corrected colors. The magnitude errors used throughout this paper are the quadratic sum of the aperture corrected color errors and the H -band MagAuto error computed by Source Extractor. The final magnitudes, corrected for Galactic extinction following Schlafly & Finkbeiner (2011), are reported in Table 1 and shown in Figure 2.

2.4. NIR Spectroscopy

A NIR spectrum of the galaxy was acquired in $0''.6$ seeing with the FIRE spectrograph (Simcoe et al. 2013) on the Magellan Baade telescope. In total, 7 hours of integration were obtained using 20 minute exposures taken in an AB dither pattern. Preliminary reduction of the data was completed with the publicly available reduction pipeline FIREHOSE.¹ The flat field was derived from internal quartz flats and the illumination correction was computed from twilight flat exposures. The initial wavelength solution from FIREHOSE utilizes both ThAr arc exposures as well as OH emission lines captured in the science exposures. The data were also flux calibrated and corrected for telluric absorption using observations of A0V stars.

Custom reduction software was developed to produce a rectified 2D spectrum (see Newman et al. 2015). The trace of the object through the echelle orders was mapped using observations of telluric calibration stars and each echellogram was rectified. Spatial object profiles were derived from the spectral regions surrounding the $[\text{O III}]$ emission lines detected in the FIREHOSE-derived sky-subtracted combined exposures for the A and B positions from each night. These profiles were used to model the contributions to the 2D spectrum from the source for second-pass sky subtraction. The wavelength solution was refined outside of FIREHOSE using OH lines in the observed data. Individual exposures were aligned and averaged without weighting, and the 1D spectrum was extracted with a boxcar of $1''.0$ width. The resultant spectrum was renormalized to match the H -band photometry and the best-fit SED template in order to correct for possible slit losses and errors in the spectrophotometry. The reduced spectrum is shown in Figure 3.

¹ Written by Rob Simcoe, John Bochanski, and Mike Matejek. <http://www.firespectrograph.org/>

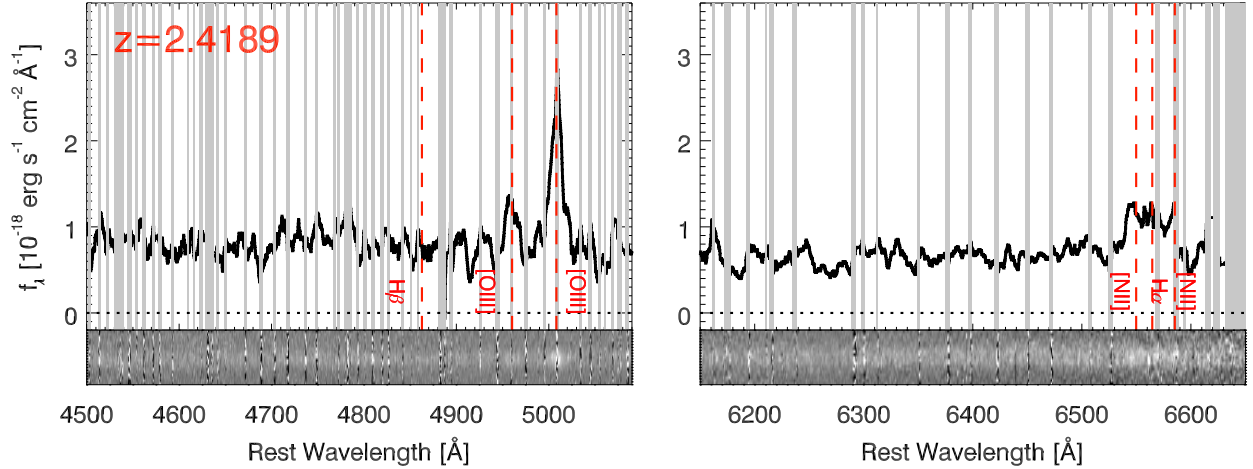


Figure 3. *H* (left) and *K* (right) band portions of the FIRE spectrum of the galaxy. The top panels show the smoothed 1D spectrum with relevant emission lines marked. The bottom panel shows the 2D spectrum.

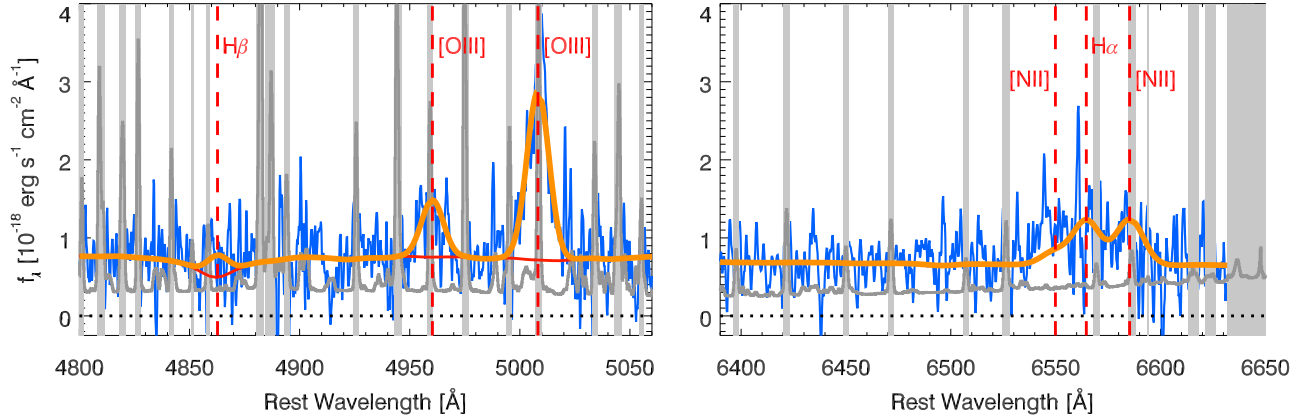


Figure 4. Gaussian fits to the 1D spectrum in *H* (left) and *K* (right) bands. The data are shown in blue along with their 1σ errors in dark gray. Regions near night sky lines are masked in light gray and excluded from the fit. The fit is shown in orange. In *H* band, the normalized best-fit SED model used as the stellar continuum in the fit (see text) is shown in red.

2.5. Photometric Modeling

The spectral energy distribution (SED) fitting code FAST (Kriek et al. 2009) was used to model the photometry of the galaxy using the Bruzual & Charlot (2003) stellar populations synthesis models, a Chabrier (2003) IMF, and a Calzetti et al. (2000) dust attenuation curve. As the spectral library does not include emission lines, we also correct the *H*-band photometry by 0.045 mag to account for the presence of $[\text{O III}] \lambda\lambda 5008, 4960$ line emission, the strongest line present in the FIRE spectrum (see Section 2.6). The redshift was fixed to the measured spectroscopic redshift of the galaxy $z_{\text{spec}} = 2.42$. The best-fit model derived by FAST implies that the galaxy is relatively massive, $\log(M/M_\odot) = 10.74^{+0.18}_{-0.16}$, with a comparatively modest star formation rate (SFR), $7^{+17}_{-4} M_\odot \text{ yr}^{-1}$, and a relatively evolved stellar population (age = 700^{+700}_{-300} Myr). The photometric data as well as the best-fit SED are shown in Figure 2.

2.6. Spectroscopic Modeling

Rest-optical spectroscopy of the galaxy (Figure 3) reveals broad $[\text{O III}]$ emission in the *H* band and blended $\text{H}\alpha$ and $[\text{N II}]$ emission in the *K* band. The *H*-band portion of the spectrum was modeled using a single Gaussian emission component for each of the $[\text{O III}] \lambda\lambda 5008, 4960$ and $\text{H}\beta$ emission lines superimposed on the best-fit stellar continuum model from the SED fitting. The best-fit SED model spectrum was convolved with a Gaussian matched to the measured $[\text{O III}]$ emission line width ($\sigma = 300 \text{ km s}^{-1}$). This model continuum was used to account for stellar absorption at $\text{H}\beta$. The emission lines were all forced to have the same redshift and velocity dispersion, and the $[\text{O III}]$ emission line fluxes were forced to have a $[\text{O III}] \lambda 5008 / \lambda 4960$ ratio of 2.98 in agreement with their theoretically determined magnetic-dipole transition probabilities (Storey & Zeippen 2000). Regions around bright night sky lines were masked prior to fitting (gray regions in Figure 4). The resulting fit is shown in the left-hand panel of Figure 4 and the parameters of the fit are listed in Table 2.

Both [O III] lines are well-detected and best fit by a broad Gaussian with $\sigma = 303 \pm 12 \text{ km s}^{-1}$ at $z = 2.4189 \pm 0.0001$. Using the best-fit SED spectrum as the model continuum yields a formal 4.8σ detection of $H\beta$; however, given the uncertainty in the precise age of the stars and the stellar velocity dispersion of the galaxy, and therefore the shape and normalization of the underlying $H\beta$ absorption, we consider one additional model to determine the maximum allowable $H\beta$ line flux. We fix all of the input parameters in FAST to the best-fit values, but set the age to $10^{8.5} \text{ yr}$, and a short exponential star-formation timescale $\tau = 10^7 \text{ yr}$ in order to produce a spectrum with the largest plausible stellar absorption at $H\beta$.² Fitting the H -band spectrum using this maximal- $H\beta$ model as the continuum results in a fit with higher $H\beta$ line flux; however, the change is smaller than the error in the fit using the best-fit SED.

[N II] $\lambda\lambda 6549, 6585$ and $H\alpha$ emission is also detected at lower significance and is more difficult to model robustly. Because of this we use a model similar to the one above, with single Gaussian components for [N II] and $H\alpha$ superimposed on the stellar continuum; however, we force the redshift and velocity dispersion of the emission lines to match that determined by the H -band fit (Figure 4, right panel). As with [O III], we fix the ratio of the [N II] emission lines to their theoretically determined [N II] $\lambda 6585/\lambda 6549$ ratio of 3.05. This results in a fit which appears to under-predict the emission at wavelengths shorter than that of $H\alpha$. The detected excess emission could be due to additional $H\alpha$ emission which is blue-shifted with respect to the main $H\alpha$ component; however the quality of the K -band data do not warrant a multi-component fit to this emission. The parameters of both the H and K -band fits are listed in Table 2.

3. THE NATURE OF J1439B

Given the close separation ($4''.7$, 38 physical kpc) of the galaxy J1439B to the high-metallicity, CO-bearing DLA seen in the spectrum of QSO J1439+1117, the properties of the galaxy are of considerable interest. In particular, it is necessary to assess the possibility that the galaxy could have a causal relationship with the DLA in which the gas represents the ejected or stripped interstellar medium (ISM) of J1439B. Given this, signatures of past feedback within the galaxy, as well as its present capability to launch gas, are of relevance. As will be shown, the galaxy sits below the main sequence of star formation, has broad nebular line emission plausibly due to an outflow, appears likely to host an AGN, and is massive enough to have enriched its ISM to near solar metallicity, consistent with the abundances derived for DLA_{J1439}. Collectively, these properties suggest J1439B is the likely source of the DLA gas.

3.1. The Position of J1439B with Respect to the Main Sequence of Star Formation

Many authors have noted star-forming galaxies exhibit a correlation between their stellar mass and star-formation rate such that high-mass galaxies typically exhibit higher levels of star formation, both in the local universe and at high

² The Bruzual & Charlot (2003) models have a maximum $H\beta$ absorption equivalent width at an age of $10^{8.5} \text{ yr}$.

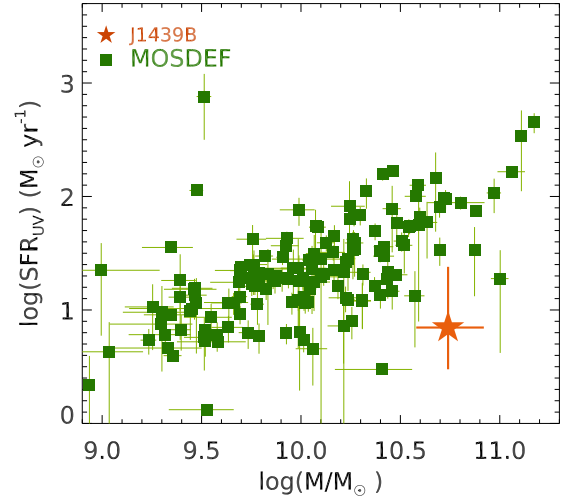


Figure 5. The SFR-stellar mass relation for $z \simeq 2$ galaxies. In green squares are shown galaxies with $2.0 < z < 2.6$ from the MOSDEF sample from Shivaee et al. (2015). The plotted values are SFRs determined from the dust-corrected UV luminosity at 1600\AA which are more analogous to the SED-determined SFR for J1439B. The same qualitative picture would hold if $H\alpha$ -based SFRs were used for the MOSDEF sample. The galaxy J1439B is plotted as the red star. Compared with typical star-forming galaxies from MOSDEF, at fixed stellar mass, J1439B exhibits significantly lower levels of star formation.

redshift (Brinchmann et al. 2004; Noeske et al. 2007; Daddi et al. 2007; Rodighiero et al. 2011; Wuyts et al. 2011; Reddy et al. 2012; Whitaker et al. 2012). Generally referred to as the “main sequence” of star formation following Noeske et al. (2007), the underlying meaning of this relation and its evolution is debated (c.f. Peng et al. 2010b; Kelson 2014; Abramson et al. 2014); however, the existence of such a correlation allows one to infer how “typical” a given SFR is for a galaxy at fixed stellar mass and redshift.

Shown in Figure 5 is a recent measurement of the main sequence of $z > 2$ galaxies from the H -band selected MOSDEF sample as presented in Shivaee et al. (2015).³ As we determine the SFR of J1439B based on the best-fit SED, the values plotted from the MOSDEF sample are those based on photometrically derived SFRs; however, the results are unchanged if one considers $H\alpha$ -based SFRs. Also plotted for comparison is the SED-based SFR and stellar mass of J1439B.⁴ It is evident from this figure that J1439B has an atypically low rate of star-formation given its present stellar mass.

3.2. The Ionization Properties of J1439 from Optical Emission Line Ratio Diagnostics

The deep rest-optical spectrum of J1439B provides important constraints on the source of ionization in the

³ Shivaee et al. (2015) measure a completeness limit of $M_* = 10^{9.5} M_\odot$. For galaxies with masses comparable to J1439B, the sample should be highly complete.

⁴ We argue below that the dominant ionization source in J1439B is an AGN, and so we refrain from reporting a SFR determined from $H\alpha$ emission. The SED-derived star-formation rate implies significantly less flux in the $H\alpha$ emission line than is measured, consistent with the argument that the SED is mostly determined by the stellar properties while the ionizing emission lines are dominated by an AGN.

Table 2
Emission Line Fit Parameters

Redshift	$\sigma_{[\text{O III}]}$ [km s ⁻¹]	Line Flux [10 ⁻¹⁸ erg s ⁻¹ cm ⁻²]				Line Ratios	
		[O III] λ 5008	H β^a	H α	[N II] λ 6585	[O III] λ 5008/H β^a	[N II] λ 6585/H α
2.4189 ± 0.0001	303 ± 12	93.5 ± 3.5	11.7 ± 2.4	38.6 ± 3.7	34.2 ± 4.0	8.0 ± 1.7	0.88 ± 0.13

^a This fit reflects the use of the best-fit SED as the continuum in order to correct for underlying stellar absorption. Without this correction, H β is undetected.

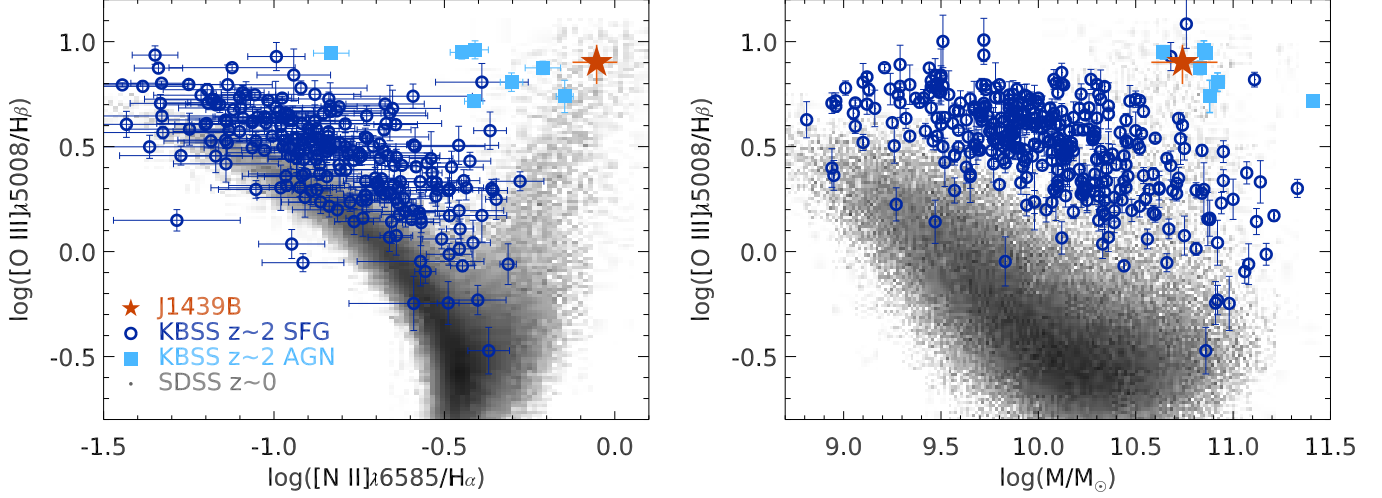


Figure 6. The BPT (left) and mass-excitation (MEx, right) diagrams for $z \approx 0$ and $z \approx 2$ galaxies. Low-redshift galaxies from the SDSS are shown in gray. In blue circles are plotted $z \approx 2$ star-forming galaxies from the KBSS (Strom et al. 2017). Galaxies spectroscopically identified to be AGN within the KBSS are plotted as blue squares. The galaxy J1439B is represented by the red star. J1439B has very high excitation (high [O III]/H β), among the highest in the KBSS sample. Given its high mass and high value of [O III]/H β and likely [N II]/H α , the galaxy J1439B likely harbors an AGN.

galaxy. One of the best known diagnostics, the [N II] BPT diagram (Baldwin et al. 1981), is shown in the left-hand panel of Figure 6. Local galaxies, taken from the SDSS Data Release 7 (Abazajian et al. 2009) are shown in the grey shading. The high-density arc of galaxies extending from the bottom middle of the plot towards the upper left is a sequence of low- z star-forming galaxies in which [O III]/H β increases and [N II]/H α decreases with decreasing gas-phase metallicity and increasing ionization. Galaxies that lie in the more diffuse distribution have optical line emission that is dominated by ionization from an AGN and the region in between is populated by galaxies with both AGN and star-formation, or those whose ionization is dominated by shocks or hot evolved stars (Veilleux & Osterbrock 1987; Kewley et al. 2001; Kauffmann et al. 2003).

Overplotted in blue are a large sample of UV-selected $z \approx 2.3$ star-forming galaxies from the Keck Baryonic Structure Survey (KBSS, Strom et al. 2017). From the KBSS sample, we plot galaxies with $> 5\sigma$ measurements of H α , $> 3\sigma$ measurements of [O III] λ 5008 and H β , and $> 2\sigma$ measurements of [N II] λ 6584. Galaxies that are spectroscopically identified as AGN are plotted in light blue squares while galaxies without such an identification are plotted as dark blue open circles. As described in Steidel et al. (2014) and Strom et al. (2017), galaxies are identified as AGN based on strong detections of high-ionization emission lines in their rest-UV spectrum (e.g. N V λ 1240, C IV λ 1549) or, for those galaxies lack-

ing rest-UV spectroscopy, unambiguous combinations of rest-optical line widths and ratios characteristic of AGN.

The location of J1439B within this diagram is represented by the red star. As had been discussed extensively in the literature (Masters et al. 2014; Steidel et al. 2014; Shapley et al. 2015; Sanders et al. 2016b; Strom et al. 2017), based on large high-redshift galaxy samples, there is clearly a systematic offset between the $z \approx 2$ and $z \approx 0$ star-forming loci. Given the higher level of ionization of high- z galaxies, and the possibility of metal-poor AGN, it is likely that the [N II] BPT diagram no longer provides a clean separation for all galaxies and AGN (Kewley et al. 2013). Coil et al. (2015) and Azadi et al. (2017) argue based on the MOSDEF sample, which includes IR and X-ray selected AGN, that some AGN may contaminate galaxies in the star-forming sequence of the BPT diagram, but that galaxies at the plotted position of J1439B are almost certainly AGN. Simply considering Figure 6, based on the location of either low- or high-redshift AGN, the position of J1439B is quite clearly within the AGN portion of the diagram. However, caution is still warranted given the lower S/N of the FIRE spectrum in the K band and the resulting poor emission line model fit. The measured ratio of [N II] λ 6585/H α is higher than all of the KBSS $z \approx 2$ galaxies; however, the measurement is likely subject to additional systematic uncertainties.⁵

⁵ The plotted error is based solely on the errors in the fit parameterized as discussed in Section 2.6. No source of systematic error due to the choice of model is taken into account.

To diagnose the likely presence of an AGN without relying on the comparatively poor quality of the K -band spectrum, we also consider a Mass-Excitation Diagram (MEx, Juneau et al. 2011) in the right-hand panel of Figure 6. The same samples are plotted as described above, but the requirements of a detection of $[\text{N II}]$ among the KBSS sample is relaxed. As was the case with the BPT diagram, the position of J1439B in the MEx diagram is most similar to the most extreme AGN in the low- z universe and coincident with all of the high- z AGN from the KBSS. While neither of these diagnostics are completely conclusive as to the nature of the ionization source, it appears likely that the galaxy hosts an AGN.

3.3. Emission Line Width

Another distinguishing property of the optical spectrum of J1439B is the large velocity dispersion $\sigma = 303 \pm 12 \text{ km s}^{-1}$ measured in the $[\text{O III}]$ emission lines. This value of σ is larger than all of the galaxies in the UV-selected KBSS-MOSFIRE sample⁶ (Strom et al. 2017), even those galaxies with significantly higher inferred stellar mass (see Figure 7). Measured values of $\sigma \gtrsim 300 \text{ km s}^{-1}$ do exist among high redshift samples, most of which fall into two distinct types: compact star-forming (c.f. van Dokkum et al. 2015) and quiescent (c.f. van Dokkum et al. 2009; Belli et al. 2017) galaxies, and AGN (c.f. Förster Schreiber et al. 2014; Genzel et al. 2014; Coil et al. 2015; Azadi et al. 2017).

In order to quantify the expected contribution to the measured $[\text{O III}]$ emission line width from virial motions of the gas within the galactic potential, we calculate the “expected velocity dispersion” following van Dokkum et al. (2015) using photometrically-derived quantities. We use *galfit* (Peng et al. 2002, 2010a) to model the H -band image using a Sersic profile + sky. The limited depth and ground-based seeing in the H -band image prevent a high-confidence fit; however, the best-fit models are disk-like, with semi-major $R_e = 3.1 \text{ kpc}$ and axis ratio $q = 0.3 - 0.4$ depending on whether we allow the Sersic index to vary or if we keep it fixed at $n = 1$. We compute a circularized half-light ratio,

$$\log(R_{e,c}) = \log R_e + 0.5 \log q \quad (1)$$

yielding $R_{e,c} = 1.8 - 1.9 \text{ kpc}$. Next we calculate the expected velocity dispersion:

$$\log(\sigma_{\text{predict}}) = 0.5(\log M_{\text{star}} - \log R_{e,c} - 5.9), \quad (2)$$

where σ_{predict} , M_{star} , and $R_{e,c}$ have units of km s^{-1} , M_{\odot} , and kpc respectively. The predicted velocity dispersion of J1439B is $\sigma_{\text{predict}} = 190 - 200 \text{ km s}^{-1}$, roughly 100 km s^{-1} less than the spectroscopically measured velocity dispersion. Given this, below we explore the likelihood that the kinematics of the gas reflect the dynamical properties of the stars within the galaxy or that of an AGN driven wind.

3.3.1. Broad Emission Lines in Compact Galaxies

A decade ago, deep HST imaging uncovered a significant population of massive compact galaxies at high redshift (c.f. Trujillo et al. 2006; van Dokkum et al.

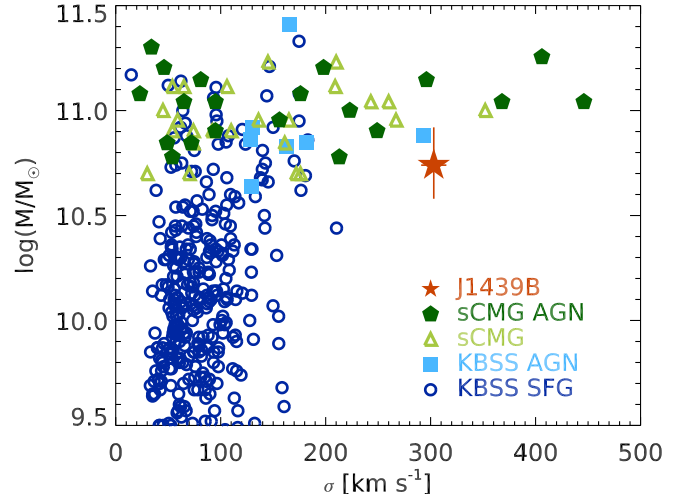


Figure 7. The ionized gas velocity dispersion - stellar mass relation for $z \simeq 2$ galaxies. $[\text{O III}]$ emission line velocity dispersions from the UV-selected star-forming galaxies from the KBSS (Strom et al. 2017) are plotted in blue, with those that are identified as AGN in light blue squares. $\text{H}\alpha$ -based velocity dispersions from the star-forming compact massive galaxies (sCMGs) described in van Dokkum et al. (2015) are shown in green with X-ray detected AGN shown as the dark green pentagons. The galaxy J1439B has a high measured $\sigma = 303 \pm 12 \text{ km s}^{-1}$, higher than all the measured σ of the KBSS. Even among the compact star-forming sample, the majority of galaxies with $\sigma > 300 \text{ km s}^{-1}$ have X-ray detected AGN.

2008). More recently, the remarkably concentrated nature of these sources was confirmed with stellar velocity dispersion measurements (van Dokkum et al. 2009; Toft et al. 2012; van de Sande et al. 2013; Belli et al. 2014; Hill et al. 2016; Barro et al. 2016; Belli et al. 2017), many of which are comparable to or larger than that of J1439B.

van Dokkum et al. (2015) targeted a sample of plausible star-forming progenitors of these systems, characterized by compact sizes, large stellar masses, and high star-formation rates. The authors followed up galaxies that had photometrically predicted velocity dispersions, $\sigma_{\text{predict}} > 250 \text{ km s}^{-1}$, finding spectroscopic velocity dispersions measured in the ionized gas that vary greatly from system to system. Specifically, van Dokkum et al. (2015) obtained K -band spectroscopy for 25 star-forming compact massive galaxies (sCMG) and measured the velocity dispersion using $\text{H}\alpha$ emission (see Figure 7). Even among this sample selected on properties expected to obtain high velocity dispersions, only five galaxies have measured emission-line velocity dispersions $\sigma \simeq 300 \text{ km s}^{-1}$, comparable to that of J1439B, four of which are X-ray detected AGN with $L_X > 10^{43} \text{ erg s}^{-1}$. van Dokkum et al. (2015) argue that the velocity dispersion of those systems are likely affected by the presence of the AGN either through winds or the dynamics of gas close to the black hole⁷.

Without a measurement of the stellar velocity dispersion in J1439B, it is not possible to rule out com-

⁶ The only galaxy with a comparable velocity dispersion is Q0821-BX101 which Steidel et al. (2014) identify as an AGN.

⁷ Note that broad $\text{H}\alpha$ emission could plausibly originate in the broad-line regions (BLR) close to a black hole; however, collisionally-excited forbidden emission such as $[\text{O III}]$ is not expected from a BLR due to the higher gas densities (see, e.g., Sulentic et al. 2000).

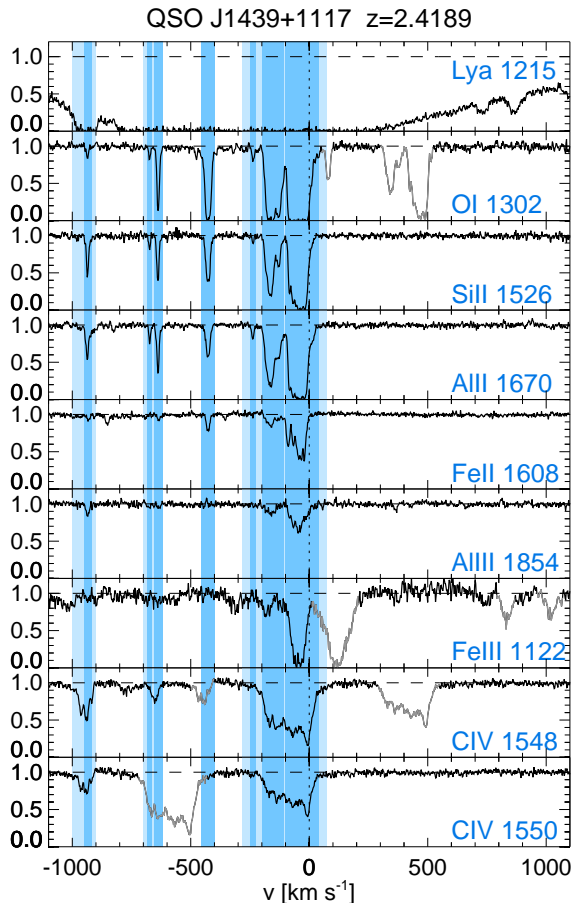


Figure 8. The continuum-normalized QSO spectrum centered on the redshift of the galaxy J1439B. Portions of the spectrum that are contaminated by metal lines from gas at a different redshift are plotted in gray. In light blue shading are highlighted the spectral regions with high-ionization absorption (C IV); in the darker shade are highlighted the regions with low-ionization metal-line absorption. High-ionization absorption in C IV is strongest at the redshift of J1439B. The center of the DLA and the highest column density low-ionization absorption is at -65 km s^{-1} with respect to J1439B. High-ionization absorption is found at velocities $-1000 < v < 75 \text{ km s}^{-1}$ and low-ionization absorption is found over the range $-950 < v < 40 \text{ km s}^{-1}$.

pletely that the measured [O III] emission line width is due to virialized motion alone. Nonetheless the argument above, combined with the high incidence of AGN among the studied population of star-forming galaxies with $\sigma \simeq 300 \text{ km s}^{-1}$, further suggests that J1439B contains an AGN and that the kinematics of the ionized gas may be due to a wind.

3.3.2. Broad Forbidden-Line Emission due to an AGN-Driven Outflow

Broad emission lines in the optical spectrum of a galaxy are often an indication of the presence of an AGN. Typically, the broadest line emission is found in the Balmer lines and originates within the broad line region (BLR), thought to be a disk of gas in orbit around the black hole. Such regions do not exhibit collisionally-excited emission lines such as [N II] and [O III] (Sulentic et al. 2000), presumably because the densities within the disk are too high to produce forbidden emission. Given the poor fit to the region surrounding $H\alpha$ and very low level emission at $H\beta$ in the

J1439B spectrum (see Section 2.6 and Figure 4), very broad Balmer line emission cannot be ruled out; however, the relatively high velocity dispersion measured for the [O III] $\lambda 5008$ emission must also be explained and does not originate from a BLR.

Förster Schreiber et al. (2014) and Genzel et al. (2014) reported the high incidence of broad emission components associated with the nuclei of $z \simeq 2$ high-mass star-forming galaxies which they interpret as signatures of AGN driven outflows. The broad components are measured in recombination emission ($H\alpha$) as well as forbidden transitions ([N II] and [S II]), suggesting they are more likely due to winds than the BLR. Genzel et al. (2014) report that 2/3 of galaxies with $\log(M/M_\odot) \gtrsim 10.9$ exhibit nuclear emission with line widths in the range of $190 \lesssim \sigma \lesssim 2250 \text{ km s}^{-1}$. Newman et al. (2012b) found that lower-mass star-forming galaxies also often exhibit underlying broad forbidden and recombination emission which they also interpret as being due to outflows; however, this emission appears to extend across the whole galaxy, has lower typical line widths $\langle \sigma \rangle \simeq 160 \text{ km s}^{-1}$, and is more likely driven by intense star formation. As J1439B has a relatively low SFR, if the broad [O III] emission is due to winds, it is unlikely that the winds are driven by star formation alone.

Genzel et al. (2014) also found that the width of the broad nuclear emission appears to correlate with the position of the galaxy above or below the star forming main sequence. Specifically, Genzel et al. (2014) stacked the nuclear spectrum of galaxies in 3 bins of stellar mass and 2 bins of star-formation rate (above and below the main sequence). For their stack of galaxies with $10.6 < \log(M/M_\odot) < 10.9$ with measured SFR that places them below the main sequence, consistent with the photometrically derived properties of J1439B, the average measured velocity dispersion of the broad nuclear component is $\sigma \simeq 290 \text{ km s}^{-1}$, very similar to the measured line width of the [O III] emission in the FIRE spectrum of J1439B.

Given the high frequency of AGN in galaxies with masses comparable to J1439B, the likelihood that the large measured emission-line velocity dispersion of J1439B is caused by outflowing winds, and the lower-than-typical star formation rate of J1439B, one must consider the possibility that DLA_{J1439} was expelled from the ISM of J1439B in a previous episode of feedback or through stripping.

3.4. The Metallicity of DLA_{J1439} and Implications for Its Relationship to Galaxy J1439B

There are many remarkable properties of DLA_{J1439}, but one of the most discriminatory as to the likely origin of the gas is its metallicity. Metal line absorption associated with the DLA is detected from a wide variety of elements and arises from gas with a large range of ionization states (see Figure 8). As the O I absorption associated with the trough of the DLA is saturated, a direct determination of the O/H ratio is not possible. However, Noterdaeme et al. (2008) report a sulfur abundance based on fits to the S II absorption components of [S/H] = -0.03 ± 0.12 . The ratio of S/O is constant across galactic environments (Pagel 2009), and so sulfur can be used as a proxy for oxygen abundance.

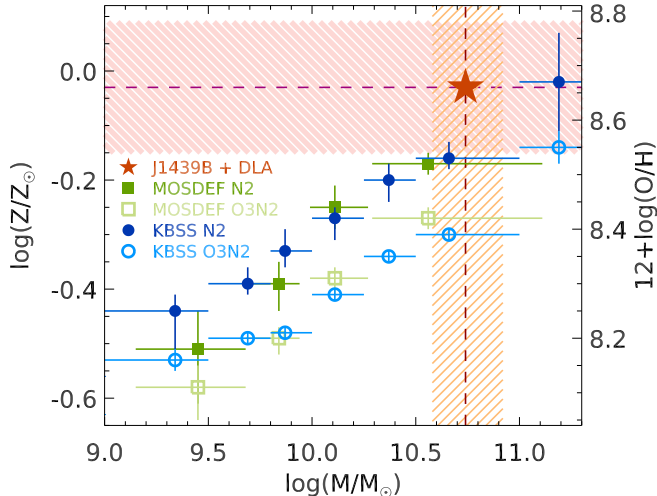


Figure 9. The mass-metallicity relation (MZR) for $z \simeq 2$ galaxies. The range of $[S/H]$ metallicity (a proxy for $[O/H]$) measured for DLA_{J1439} is shown as the horizontal line and the pink shaded horizontal region is the error from Noterdaeme et al. (2008). For comparison, also shown are masses and $12 + \log(O/H)$ (right axis) for two samples of star-forming galaxies with comprehensive NIR spectroscopy. In blue is shown the MZR for the KBSS sample as presented in Steidel et al. (2014) using the N2 (dark blue filled circles) and O3N2 (light blue open circles) strong line metallicity indicators. In green squares are shown the analogous data from the MOSDEF survey as presented in Sanders et al. (2015). While there still exists considerable uncertainty in the MZR at $z \simeq 2$, it is clear that solar metallicity gas is uncommon in systems with $\log(M/M_\odot) \ll 11$. The best-fit and range of stellar masses derived from the photometry of galaxy J1439B is shown in the orange shading and vertical dashed line. Combining the DLA-derived metallicity and the stellar mass of J1439B (assuming the DLA represents the ISM of the galaxy) would give the red star. The location of the data point for J1439 in comparison to the MZR of the $z \simeq 2$ samples is consistent with the possibility that the DLA gas could be ejected ISM from J1439B.

There is considerable uncertainty regarding the true oxygen abundance of the ISM of high-redshift galaxies. Because oxygen abundances can only be directly measured for a rare subset of galaxies at high- z (Yuan & Kewley 2009; Wuyts et al. 2012; Christensen et al. 2012; Bayliss et al. 2014; Sanders et al. 2016a), most of which are gravitationally lensed, the majority of the inferences regarding the chemical abundances of distant galaxies are based on the ratios of ionization and excitation sensitive emission line ratios such as N2, O3N2, and R_{23} (see, e.g., Pettini & Pagel 2004). Unfortunately, these metallicity diagnostics introduce systematic uncertainties as large as 0.7 dex *even in the local universe* (Kewley & Ellison 2008). Further, the typical emission line ratios of star-forming galaxies evolve with redshift (see Section 3.2) which manifest as large discrepancies in the abundances derived for the *same high- z galaxy* using different strong line diagnostics (Steidel et al. 2014; Sanders et al. 2015). Thankfully, even given these considerable caveats, the high level of enrichment of the DLA is constraining because all determinations of the high- z mass-metallicity relation suggest that solar metallicity enrichment only occurs in very massive galaxies.

Figure 9 shows the most recent determinations of the mass-metallicity relation of $z \simeq 2$ star-forming

galaxies based on statistical samples with uniform data. We consider metallicities determined from both the N2 (filled symbols) and O3N2 (open symbols) indicator as measured in the H -band selected MOSDEF sample (Sanders et al. 2015, green squares) and the UV-selected KBSS sample (Steidel et al. 2014; blue circles). For comparison, in pink shading, we show the constraints on the α abundance of the DLA. Clearly, whichever galaxy responsible for the absorption system must have a high stellar mass capable of producing roughly solar metallicity enrichment. The mass of J1439B, indicated by the orange vertical shading, is consistent with the possibility that the DLA is ejected or stripped ISM from the galaxy.

4. DISCUSSION

4.1. Could Another Galaxy be Responsible for DLA_{J1439}?

As outlined above, there is considerable evidence of a plausible connection between the galaxy J1439B and the DLA_{J1439}. However, if J1439B is the galaxy counterpart to the DLA, it is the widest separation thus far known between a galaxy and an absorber with $N_{\text{HI}} > 10^{20} \text{ cm}^{-2}$ at $z > 2$ (Fumagalli et al. 2015). Here we explore the possibility that another galaxy could be responsible for the DLA.

In Section 3.4 and Figure 9, we showed that the DLA's high metallicity implies the source of its enrichment is likely a massive galaxy with mass comparable to or greater than that of J1439B. The images shown in Figure 1 rule out the existence of another galaxy with comparable mass to J1439B lying closer to the line of sight to the QSO unless the galaxy is hidden within the PSF of the QSO.⁸

Additional constraints on the existence of a galaxy very close to the line of sight to the QSO were discussed in Bouché et al. (2012) using data from the z2SIMPLE survey taken with the Spectrograph for INTEGRAL Field Observation in the Near-Infrared (SINFONI; Eisenhauer et al. 2003) on the VLT. Bouché et al. (2012) took K -band IFU spectroscopy in natural seeing of a $10'' \times 10''$ field surrounding 28 QSOs, including QSO J1439+1117. Among their 28 absorbers, they detected only 4 possible host galaxies and did not detect a galaxy at the redshift of DLA_{J1439}.⁹

In the central $4''$ search area surrounding the QSOs, Bouché et al. (2012) report a 5σ limiting $H\alpha$ flux of $2.3 \times 10^{-17} \text{ erg s}^{-1} \text{ cm}^{-2}$ corresponding to a 5σ limiting SFR of $3.9 M_\odot \text{ yr}^{-1}$ uncorrected for dust, integrated over 8 spectral pixels or roughly 300 km s^{-1} . For a galaxy analogous to J1439B with an emission line velocity dispersion $\sigma = 300 \text{ km s}^{-1}$, the true limit is somewhat less stringent as the line emission would be spread over a larger number of pixels. Nevertheless, the SINFONI data

⁸ The H -band image of J1439B provides a 14σ detection of the galaxy. As this corresponds to rest-frame $\sim 5000\text{\AA}$, the luminosity is a good proxy for mass. We would detect a galaxy of comparable size but 5 times less luminous at 3σ . The other source directly east of J1439B that is visually apparent in Figure 1 has a photometric redshift computed with EAZY (Brammer et al. 2008) inconsistent with solutions $z > 2$. No other faint galaxies are detected with separations $< 5''$ from the QSO.

⁹ The position of J1439B is very near the edge of the field of view of the SINFONI observations and only received half the exposure time.

further demonstrate the lack of a galaxy closer to the line of sight. Bouché et al. (2012) argue that only within a $0''.3$ radius of the QSO would the SINFONI data been insensitive to the $H\alpha$ emission from the galaxy.

The final possibility is that another galaxy lies directly on top of the line of sight to the QSO and has an unfavorable contrast ratio, leaving it undetected in the imaging and IFU observations. This is a challenging possibility to disprove, but we can quantify the likelihood in part using measurements of the pair fraction of massive $z \simeq 2$ galaxies.

There have been several studies aimed at quantifying the merger rate at high redshift that have measured the fraction of massive galaxies that are found with close companions. In this work, we are most interested in pairs of nearly equal mass since, as we argue in Section 3.4, the metallicity of DLA_{J1439} indicates the source of its metals is likely a galaxy of mass equal to or greater than than of J1439B. Given this, we consider the results of studies qualifying the pair fraction of 1/4 mass ratio pairs to be an upper limit on the likelihood that another galaxy would be the primary origin of the absorber. Three recent studies have considered the incidence of satellites surrounding massive $\log(M/M_\odot) > 10.54 - 11$ galaxies with $1.5 < z < 3.0$ and projected separations less than ~ 40 kpc, finding that 7 – 15% of such galaxies have a likely companion at least 1/4 as massive as the primary (Newman et al. 2012a; Man et al. 2012, 2016).

In practice, we are only interested in the volume surrounding the galaxy that is closer to the line of sight to the QSO, and we have ruled out the existence of such a galaxy in the majority of that volume, but not at the precise location of the QSO line of sight. Further, we have argued that galaxies with $\log(M/M_\odot) \ll 11$ are unlikely to be responsible for the high levels of chemical enrichment found in the DLA. Given these caveats, we consider 7 – 15% to be a very conservative upper limit on the probability that another galaxy is responsible for DLA_{J1439}.

4.2. Implications

If DLA_{J1439} represents the ejected or stripped ISM of J1439B, it offers a rare window into the properties of the ISM in high- z galaxies. As shown in Figure 8, metal-line absorption associated with the DLA is spread over $\Delta v > 1000$ km s⁻¹ both in low and high ionization gas. Given the large velocity spread, we favor a wind scenario as the likely explanation over stripping, implying that DLA_{J1439} also provides a unique view of AGN-driven winds at high redshift.

4.2.1. The Chemical Evolution of J1439B

The detailed elemental abundances of DLA_{J1439} provides insight into the nature of the ISM within the source galaxy. Si and Fe absorption is measured and their abundances show similar levels of depletion as is typical of the Galactic ISM (Srianand et al. 2008). The abundances of S and Zn, which are typically not depleted onto dust grains, are consistent with a high level of enrichment, roughly solar metallicity ($[S/H] = -0.3 \pm 0.12$, $[Zn/H] = +0.16 \pm 0.11$), and their ratios can be used to measure the level of α -enhancement. In DLA_{J1439} the gas is consistent with solar α/Fe (Noterdaeme et al. 2008).

This is notable given the significant α -enhancements that are common in the old stars within giant elliptical galaxies (Worthey et al. 1992; Henry & Worthey 1999; Trager et al. 2000; Thomas et al. 2005), and the recent finding of super-solar O/Fe $[\simeq 4 - 5 (O/Fe)_\odot]$ in UV-selected star-forming galaxies at the same cosmic epoch (Steidel et al. 2016). Interestingly, Noterdaeme et al. (2008) argue that the N/O ratio in DLA_{J1439} also appears to be consistent with the solar ratio, again somewhat at odds with the recent determination of $[N/O] = -0.38 \pm 0.04$ in L^* star-forming galaxies at $z \sim 2$ from Steidel et al. (2016). Both the α/Fe and N/O ratios suggest a level of chemical maturity associated with prolonged star formation histories, consistent with the \sim Gyr age estimate of J1439B from the SED fitting.

4.2.2. AGN-Driven Outflows

Molecular outflows have been definitively observed in several local AGN and QSOs (Feruglio et al. 2010; Alatalo et al. 2011; Sturm et al. 2011), extending in some cases over many kiloparsecs (Cicone et al. 2014). Extended outflows have also been observed in multiple phases, both in ionized (Greene et al. 2012; Liu et al. 2013a,b, 2014; Hainline et al. 2014; Sun et al. 2017; Yuma et al. 2017) and [CII]-emitting gas (Cicone et al. 2015; Maiolino et al. 2012) at both high and low redshift. Harrison et al. (2014) considered a sample of 16 $z < 0.2$ type 2 AGN, finding that all of them had ionized gas emission lines similar to those observed in J1439B with $\sigma > 300$ km s⁻¹, and that 70% of such galaxies have outflows that extend over kpc scales.

Interestingly, many authors have noted a relationship between the detected extent of the ionized outflow and the luminosity of the AGN (Liu et al. 2013a,b, 2014; Hainline et al. 2014; Sun et al. 2017). In particular, extended ionized outflows seem to be most common in AGN with $L_{\text{bol}} \gtrsim 10^{46}$ erg s⁻¹ (Sun et al. 2017). Following, Reyes et al. (2008) and Liu et al. (2009) who derive a relationship between the bolometric luminosity of AGN and the luminosity of their [O III] emission, we calculate $L_{\text{J1439B}, [\text{O III}]} = 10^{42.6}$ erg s⁻¹ $= 10^{33.6} L_\odot$ which would imply $L_{\text{J1439B}, \text{bol}} = 10^{46.0}$ erg s⁻¹. This suggests the AGN in J1439B is comparably luminous to the class of lower-redshift AGN that have been shown to drive outflows.

While clearly uncertain, it is plausible that the DLA_{J1439} represents wind material from an AGN driven outflow from J1439B. In that case, the J1439 DLA-galaxy system offers many unique clues about the nature of such a wind. In particular given the detection at 38 kpc, J1439 provides spatial information about the extent of the wind through a more sensitive probe than in emission. Additionally, the properties of the gas can be studied in much greater detail through the DLAs absorption lines, providing high-fidelity measurements of the chemistry, density, and kinematics of the gas at large distances from the galaxy.

Given the measurement of $\log(N_{\text{CO}}) = 13.89 \pm 0.02$ and $\log(N_{\text{H}_2}) = 19.38 \pm 0.10$ in this DLA by Srianand et al. (2008), it is possible to measure $N(\text{CO})/N(\text{H}_2) = 3 \times 10^{-6}$. This is significantly less than the value typical of star-forming regions in the local universe where $N(\text{CO})/N(\text{H}_2) = 2.7 \times 10^{-4}$ (Lacy et al. 1994). The ra-

tio is comparable to values observed in diffuse clouds in the Galaxy, but at fixed $\log(N_{\text{H}_2})$, DLA_{J1439} has 0.5–1 dex more CO (Burgh et al. 2007; Sheffer et al. 2008). Using the ratio of fine-structure carbon absorption lines, Srianand et al. (2008) also derive a density of the DLA to be $45 - 62 \text{ cm}^{-3}$, comparable to, although somewhat lower than, the typical densities in diffuse clouds within the ISM of the Milky Way (Snow & McCall 2006). Taken together, these two measurements suggest that the physical properties of the gas are likely similar to that of diffuse Galactic clouds.

In addition to the properties of the gas and their implications for its physical state, the kinematics of the various absorption components are also of interest. In Figure 8, one can clearly see a number of distinct metallic absorption features. While the redshift of the galaxy $z = 2.4189$ is well aligned with the strongest components of the neutral and low-ionization gas ($z = 2.41837$, $\Delta v = 46 \text{ km s}^{-1}$), the majority of the metal line absorption systems lie blue-shifted with respect to both the DLA and J1439B, with the highest-velocity absorbers detected in low-ionization (e.g. O I, Si II) as well as high-ionization (e.g. C IV) lines extending to ~ 950 and $\sim 1000 \text{ km s}^{-1}$ respectively. Redshifted metal lines extend to less than 100 km s^{-1} in the opposite direction.

The large velocity spread of the metal-line absorbers detected in the QSO spectrum require a fast outflow with $v \gtrsim 1000 \text{ km s}^{-1}$, again suggestive of AGN-driven winds. Assuming an outflow model with a constant outflow velocity, the kinematics of the absorbing gas provide a joint constraint on the opening angle of the outflow and the outflow velocity. For an outflow velocity of 3000 km s^{-1} or less, the opening angle would be larger than 20 degrees.

The presence and high fraction of molecular gas within the DLA [$f = 2N(\text{H}_2)/(N(\text{H I}) + 2N(\text{H}_2)) = 0.27^{+0.10}_{-0.08}$; Srianand et al. 2008] is also of considerable interest. In particular, if the absorbing gas was ejected from J1439B in its present state, it is a possible explanation for its anemic SFR given that the direct fuel for star formation would have been removed.

In addition to this, the most likely scenario is that this gas escapes completely from the halo. If we assume the stellar mass – halo mass relation from Behroozi et al. (2013), J1439B has a dark matter halo mass of $M_{\text{halo}} \simeq 10^{12.4} M_{\odot}$. The measured velocity range in the metal line absorbers ($v \simeq 1000 \text{ km s}^{-1}$) is comparable to the escape velocity of the halo at a distance of 38 kpc. So if DLA_{J1439} is the ejected ISM of J1439B, it represents the permanent removal of star-formation-ready material from a galaxy, a very effective and long-lasting form of feedback.

4.2.3. Timescales

Lastly, we comment briefly on the timescales of interest implied by the measured velocities of the wind and the distance between J1439B and the QSO line of sight. In Section 3.3.2, we argue that the large measured emission-line velocity dispersion of J1439B is most likely due to an AGN driven wind. This suggests a lower limit for the current outflowing wind speed of $\sim 300 \text{ km s}^{-1}$. Above in Section 4.2.2, we discuss the possibility of a $\gtrsim 1000 \text{ km s}^{-1}$ outflow based on the kin-

matics of the gas detected in absorption. Noting the projected distance between the galaxy and the QSO line of sight of 38 kpc, it would take $\sim 10^8$ years for gas traveling at 300 km s^{-1} to cover this distance. If that gas were instead ejected at 1000 km s^{-1} , it would require only 4×10^7 years. Either of these timescales is significantly shorter than the typical age of the stars suggested by the SED fit ($\sim 700 \text{ Myr}$). This is consistent with the high levels of enrichment measured in the DLA; a majority of the stars in the galaxy would have formed prior to the ejection of the gas, enriching the ISM to the solar metallicity value measured. Further, the travel time required is similar to the expected lifetime of AGN in the distant universe (Haiman & Loeb 1998; Haehnelt et al. 1998a; Yu & Tremaine 2002; Martini 2004; Hopkins & Hernquist 2009).

5. SUMMARY

We report the discovery of a galaxy 38 kpc from the sightline to QSO J1439+1117 coincident with the redshift of the CO-bearing, solar-metallicity sub-DLA. We presented optical and NIR photometry of the galaxies as well as SED fits which show the galaxy is massive ($\log(M/M_{\odot}) = 10.74^{+0.18}_{-0.16}$) and evolved (Section 2.5 and Figure 2). A NIR spectrum of the galaxy, J1439B, observed with Magellan/FIRE shows broad [O III] emission ($\sigma = 303 \pm 12 \text{ km s}^{-1}$) as well as [N II] and H α emission (Section 2.6 and Figure 4).

Based on the properties of the galaxy and the DLA, we argue there is a plausible connection between J1439B and DLA_{J1439}:

- The galaxy has a lower-than-typical SFR given its stellar mass, suggesting there could be some process occurring, or that occurred in the past, which prevents star formation (Section 3.1 and Figure 5).
- The ionization properties of J1439B determined from the [N II] BPT diagram and mass-excitation diagram favor the galaxy harboring an AGN (Section 3.2 and Figure 6).
- The large velocity dispersion observed in J1439B's nebular emission lines is most plausibly explained by an AGN-driven outflow (Section 3.3 and Figure 7).
- The metallicity of DLA_{J1439} requires enrichment within a high-mass, evolved galaxy, similar to J1439B (Section 3.4 and Figure 9).

In Section 4.1, we explored the possibility that another galaxy might lie closer to the line of sight and be the true galactic counterpart to the DLA. We conclude based on our imaging, as well as published IFU spectroscopy, that another massive galaxy does not lie closer to the line of sight unless it is coincident with the QSO sightline. Based on pair statistics for massive high-redshift galaxies, we conclude that there is no more than a 15% chance that another massive galaxy lies within $\sim 40 \text{ kpc}$ of the line of sight.

We conclude that J1439B is likely the galactic counterpart of DLA_{J1439}, and that the DLA is most likely the ISM ejected by the AGN. In this scenario, the properties of DLA_{J1439} offer a rare view of the chemistry of

the ISM close to a high-redshift AGN and of the state of gas driven out by AGN feedback. The DLA has solar α/Fe and N/O abundance ratios, suggesting the galaxy is quite chemically evolved with a longer star formation history. The molecular properties of the DLA are most similar to that of diffuse clouds in the Milky Way and the large velocity spread ($> 1000 \text{ km s}^{-1}$) of associated metal line absorption imply large outflow velocities. At a distance of 38 kpc, the large velocity spread also suggests much of the absorbing material would be unbound from J1439B. Given the significant molecular gas content within the DLA, this would represent the ejection of gas that otherwise would have likely undergone star formation.

The collective properties of J1439B and $\text{DLA}_{\text{J1439}}$ are consistent with the picture in which AGN play an active role in modulating the star formation of massive, high-redshift galaxies. Confirmation of the X-ray and radio properties of J1439B would provide better understanding of the nature of the AGN and the detection of extended molecular emission would cement the connection between J1439B and $\text{DLA}_{\text{J1439}}$. These further observations provide a unique opportunity to obtain a more detailed view of AGN feedback in the high-redshift universe.

The authors wish to thank D. Kelson for the use of his FourCLift FourStar Reduction code and for his assistance with it. We acknowledge insightful discussions with J. Grenne, D. Kelson, and C. Steidel which improved the content of the paper. We also thank J. Kollmeier and S. Dong for obtaining the IMACS optical photometry of the galaxy, I. Shivaee and N. Reddy for providing the MOSDEF data plotted in Figure 5, and A. Strom for providing catalogs of the KBSS measurements.

MTM thanks the Australian Research Council for Discovery Project grant DP130100568 which supported this work. This paper includes data gathered with the 6.5-meter Magellan Telescopes located at Las Campanas Observatory, Chile as well as observations collected at the European Organisation for Astronomical Research in the Southern Hemisphere under ESO program 278.A-5062(A) and obtained from the ESO Science Archive Facility.

REFERENCES

- Abazajian, K. N., Adelman-McCarthy, J. K., Agüeros, M. A., et al. 2009, *ApJS*, 182, 543
- Abramson, L. E., Kelson, D. D., Dressler, A., et al. 2014, *ApJ*, 785, L36
- Alatalo, K., Blitz, L., Young, L. M., et al. 2011, *ApJ*, 735, 88
- Azadi, M., Coil, A. L., Aird, J., et al. 2017, *ApJ*, 835, 27
- Bagdonaite, J., Ubachs, W., Murphy, M. T., & Whitmore, J. B. 2014, *ApJ*, 782, 10
- Baldwin, J. A., Phillips, M. M., & Terlevich, R. 1981, *PASP*, 93, 5
- Barro, G., Faber, S. M., Dekel, A., et al. 2016, *ApJ*, 820, 120
- Bayliss, M. B., Rigby, J. R., Sharon, K., et al. 2014, *ApJ*, 790, 144
- Behroozi, P. S., Wechsler, R. H., & Conroy, C. 2013, *ApJ*, 770, 57
- Belli, S., Newman, A. B., & Ellis, R. S. 2014, *ApJ*, 783, 117
- . 2017, *ApJ*, 834, 18
- Benson, A. J., Bower, R. G., Frenk, C. S., et al. 2003, *ApJ*, 599, 38
- Bertin, E., & Arnouts, S. 1996, *A&AS*, 117, 393
- Bird, S., Haehnelt, M., Neeleman, M., et al. 2015, *MNRAS*, 447, 1834
- Bouché, N., Murphy, M. T., Kacprzak, G. G., et al. 2013, *Science*, 341, 50
- Bouché, N., Murphy, M. T., Péroux, C., et al. 2012, *MNRAS*, 419, 2
- Brammer, G. B., van Dokkum, P. G., & Coppi, P. 2008, *ApJ*, 686, 1503
- Brinchmann, J., Charlot, S., White, S. D. M., et al. 2004, *MNRAS*, 351, 1151
- Bruzual, G., & Charlot, S. 2003, *MNRAS*, 344, 1000
- Burgh, E. B., France, K., & McCandliss, S. R. 2007, *ApJ*, 658, 446
- Calzetti, D., Armus, L., Bohlin, R. C., et al. 2000, *ApJ*, 533, 682
- Chabrier, G. 2003, *PASP*, 115, 763
- Christensen, L., Laursen, P., Richard, J., et al. 2012, *MNRAS*, 427, 1973
- Cicone, C., Maiolino, R., Sturm, E., et al. 2014, *A&A*, 562, A21
- Cicone, C., Maiolino, R., Gallerani, S., et al. 2015, *A&A*, 574, A14
- Coil, A. L., Aird, J., Reddy, N., et al. 2015, *ApJ*, 801, 35
- Cole, S., Aragon-Salamanca, A., Frenk, C. S., Navarro, J. F., & Zepf, S. E. 1994, *MNRAS*, 271, 781
- Cooke, J., Wolfe, A. M., Gawiser, E., & Prochaska, J. X. 2006, *ApJ*, 652, 994
- Cooke, R., Pettini, M., Steidel, C. C., et al. 2010, *MNRAS*, 409, 679
- Croton, D. J., Springel, V., White, S. D. M., et al. 2006, *MNRAS*, 365, 11
- Daddi, E., Dickinson, M., Morrison, G., et al. 2007, *ApJ*, 670, 156
- Dekker, H., D’Odorico, S., Kaufer, A., Delabre, B., & Kotzlowski, H. 2000, in *Proc. SPIE*, Vol. 4008, *Optical and IR Telescope Instrumentation and Detectors*, ed. M. Iye & A. F. Moorwood, 534–545
- Dressler, A., Bigelow, B., Hare, T., et al. 2011, *PASP*, 123, 288
- Efstathiou, G. 2000, *MNRAS*, 317, 697
- Eisenhauer, F., Abuter, R., Bickert, K., et al. 2003, in *Proc. SPIE*, Vol. 4841, *Instrument Design and Performance for Optical/Infrared Ground-based Telescopes*, ed. M. Iye & A. F. M. Moorwood, 1548–1561
- Erb, D. K. 2008, *ApJ*, 674, 151
- Feruglio, C., Maiolino, R., Piconcelli, E., et al. 2010, *A&A*, 518, L155
- Finlator, K., & Davé, R. 2008, *MNRAS*, 385, 2181
- Förster Schreiber, N. M., Genzel, R., Newman, S. F., et al. 2014, *ApJ*, 787, 38
- Fumagalli, M., O’Meara, J. M., Prochaska, J. X., & Kanekar, N. 2010, *MNRAS*, 408, 362
- Fumagalli, M., O’Meara, J. M., Prochaska, J. X., Rafelski, M., & Kanekar, N. 2015, *MNRAS*, 446, 3178
- Fynbo, J. P. U., Laursen, P., Ledoux, C., et al. 2010, *MNRAS*, 408, 2128
- Fynbo, J. P. U., Ledoux, C., Noterdaeme, P., et al. 2011, *MNRAS*, 413, 2481
- Genzel, R., Förster Schreiber, N. M., Rosario, D., et al. 2014, *ApJ*, 796, 7
- Greene, J. E., Zakamska, N. L., & Smith, P. S. 2012, *ApJ*, 746, 86
- Haehnelt, M. G., Natarajan, P., & Rees, M. J. 1998a, *MNRAS*, 300, 817
- Haehnelt, M. G., Steinmetz, M., & Rauch, M. 1998b, *ApJ*, 495, 647
- Haiman, Z., & Loeb, A. 1998, *ApJ*, 503, 505
- Hainline, K. N., Hickox, R. C., Greene, J. E., et al. 2014, *ApJ*, 787, 65
- Harrison, C. M., Alexander, D. M., Mullaney, J. R., & Swinbank, A. M. 2014, *MNRAS*, 441, 3306
- Hartoog, O. E., Fynbo, J. P. U., Kaper, L., De Cia, A., & Bagdonaite, J. 2015, *MNRAS*, 447, 2738
- Henry, R. B. C., & Worthey, G. 1999, *PASP*, 111, 919
- Hill, A. R., Muzzin, A., Franx, M., & van de Sande, J. 2016, *ApJ*, 819, 74
- Hopkins, P. F., & Hernquist, L. 2009, *ApJ*, 698, 1550
- Hopkins, P. F., Quataert, E., & Murray, N. 2012, *MNRAS*, 421, 3522
- Jorgenson, R. A., Murphy, M. T., & Thompson, R. 2013, *MNRAS*, 435, 482
- Jorgenson, R. A., & Wolfe, A. M. 2014, *ApJ*, 785, 16
- Juneau, S., Dickinson, M., Alexander, D. M., & Salim, S. 2011, *ApJ*, 736, 104
- Kashikawa, N., Misawa, T., Minowa, Y., et al. 2014, *ApJ*, 780, 116

- Kauffmann, G., Colberg, J. M., Diaferio, A., & White, S. D. M. 1999, *MNRAS*, 303, 188
- Kauffmann, G., Heckman, T. M., Tremonti, C., et al. 2003, *MNRAS*, 346, 1055
- Kelson, D. D. 2014, *ArXiv e-prints*
- Kelson, D. D., Williams, R. J., Dressler, A., et al. 2014, *ApJ*, 783, 110
- Kewley, L. J., Dopita, M. A., Sutherland, R. S., Heisler, C. A., & Trevena, J. 2001, *ApJ*, 556, 121
- Kewley, L. J., & Ellison, S. L. 2008, *ApJ*, 681, 1183
- Kewley, L. J., Maier, C., Yabe, K., et al. 2013, *ApJ*, 774, L10
- Kriek, M., van Dokkum, P. G., Labbé, I., et al. 2009, *ApJ*, 700, 221
- Krogager, J.-K., Fynbo, J. P. U., Møller, P., et al. 2012, *MNRAS*, 424, L1
- Lacy, J. H., Knacke, R., Geballe, T. R., & Tokunaga, A. T. 1994, *ApJ*, 428, L69
- Lau, M. W., Prochaska, J. X., & Hennawi, J. F. 2016, *ApJS*, 226, 25
- Liszt, H. S. 2015, *ApJ*, 799, 66
- Liu, G., Zakamska, N. L., & Greene, J. E. 2014, *MNRAS*, 442, 1303
- Liu, G., Zakamska, N. L., Greene, J. E., Nesvadba, N. P. H., & Liu, X. 2013a, *MNRAS*, 430, 2327
- , 2013b, *MNRAS*, 436, 2576
- Liu, X., Zakamska, N. L., Greene, J. E., et al. 2009, *ApJ*, 702, 1098
- Maiolino, R., Gallerani, S., Neri, R., et al. 2012, *MNRAS*, 425, L66
- Man, A. W. S., Toft, S., Zirm, A. W., Wuyts, S., & van der Wel, A. 2012, *ApJ*, 744, 85
- Man, A. W. S., Zirm, A. W., & Toft, S. 2016, *ApJ*, 830, 89
- Martini, P. 2004, *Coevolution of Black Holes and Galaxies*, 169
- Masters, D., McCarthy, P., Siana, B., et al. 2014, *ApJ*, 785, 153
- Møller, P., Fynbo, J. P. U., & Fall, S. M. 2004, *A&A*, 422, L33
- Møller, P., & Warren, S. J. 1993, *A&A*, 270, 43
- Møller, P., Warren, S. J., Fall, S. M., Fynbo, J. U., & Jakobsen, P. 2002, *ApJ*, 574, 51
- Monier, E. M., Turnshek, D. A., & Rao, S. 2009, *MNRAS*, 397, 943
- Murphy, M. T. 2016, *UVES popler: POrt PipeLine Echelle Reduction software*
- Murphy, M. T., Tzanavaris, P., Webb, J. K., & Lovis, C. 2007, *MNRAS*, 378, 221
- Murray, N., Ménard, B., & Thompson, T. A. 2011, *ApJ*, 735, 66
- Neeleman, M., Wolfe, A. M., Prochaska, J. X., & Rafelski, M. 2013, *ApJ*, 769, 54
- Newman, A. B., Belli, S., & Ellis, R. S. 2015, *ApJ*, 813, L7
- Newman, A. B., Ellis, R. S., Bundy, K., & Treu, T. 2012a, *ApJ*, 746, 162
- Newman, S. F., Genzel, R., Förster-Schreiber, N. M., et al. 2012b, *ApJ*, 761, 43
- Noeske, K. G., Weiner, B. J., Faber, S. M., et al. 2007, *ApJ*, 660, L43
- Noterdaeme, P., Petitjean, P., Ledoux, C., Srianand, R., & Ivanchik, A. 2008, *A&A*, 491, 397
- Noterdaeme, P., Petitjean, P., Carithers, W. C., et al. 2012a, *A&A*, 547, L1
- Noterdaeme, P., Laursen, P., Petitjean, P., et al. 2012b, *A&A*, 540, A63
- Oke, J. B., & Gunn, J. E. 1983, *ApJ*, 266, 713
- O’Meara, J. M., Prochaska, J. X., Burles, S., et al. 2007, *ApJ*, 656, 666
- Pagel, B. E. J. 2009, *Nucleosynthesis and Chemical Evolution of Galaxies* (Cambridge University Press)
- Peng, C. Y., Ho, L. C., Impey, C. D., & Rix, H.-W. 2002, *AJ*, 124, 266
- , 2010a, *AJ*, 139, 2097
- Peng, Y.-j., Lilly, S. J., Kovač, K., et al. 2010b, *ApJ*, 721, 193
- Péroux, C., Bouché, N., Kulkarni, V. P., & York, D. G. 2013, *MNRAS*, 436, 2650
- Péroux, C., Bouché, N., Kulkarni, V. P., York, D. G., & Vladilo, G. 2011, *MNRAS*, 410, 2237
- , 2012, *MNRAS*, 419, 3060
- Persson, S. E., Murphy, D. C., Smee, S., et al. 2013, *PASP*, 125, 654
- Pettini, M., & Pagel, B. E. J. 2004, *MNRAS*, 348, L59
- Pettini, M., Shapley, A. E., Steidel, C. C., et al. 2001, *ApJ*, 554, 981
- Pettini, M., Smith, L. J., King, D. L., & Hunstead, R. W. 1997, *ApJ*, 486, 665
- Pontzen, A., Governato, F., Pettini, M., et al. 2008, *MNRAS*, 390, 1349
- Prochaska, J. X., & Wolfe, A. M. 1997, *ApJ*, 487, 73
- Rafelski, M., Wolfe, A. M., & Chen, H.-W. 2011, *ApJ*, 736, 48
- Rafelski, M., Wolfe, A. M., Prochaska, J. X., Neeleman, M., & Mendez, A. J. 2012, *ApJ*, 755, 89
- Reddy, N. A., Pettini, M., Steidel, C. C., et al. 2012, *ApJ*, 754, 25
- Reyes, R., Zakamska, N. L., Strauss, M. A., et al. 2008, *AJ*, 136, 2373
- Rodighiero, G., Daddi, E., Baronchelli, I., et al. 2011, *ApJ*, 739, L40
- Rubin, K. H. R., Hennawi, J. F., Prochaska, J. X., et al. 2015, *ApJ*, 808, 38
- Rudie, G. C., Steidel, C. C., Trainor, R. F., et al. 2012, *ApJ*, 750, 67
- Sanders, R. L., Shapley, A. E., Kriek, M., et al. 2015, *ApJ*, 799, 138
- , 2016a, *ApJ*, 825, L23
- , 2016b, *ApJ*, 816, 23
- Schlaflly, E. F., & Finkbeiner, D. P. 2011, *ApJ*, 737, 103
- Shapley, A. E., Steidel, C. C., Pettini, M., & Adelberger, K. L. 2003, *ApJ*, 588, 65
- Shapley, A. E., Reddy, N. A., Kriek, M., et al. 2015, *ApJ*, 801, 88
- Sheffer, Y., Rogers, M., Federman, S. R., et al. 2008, *ApJ*, 687, 1075
- Shivaei, I., Reddy, N. A., Shapley, A. E., et al. 2015, *ApJ*, 815, 98
- Simcoe, R. A., Burgasser, A. J., Schechter, P. L., et al. 2013, *PASP*, 125, 270
- Snow, T. P., & McCall, B. J. 2006, *ARA&A*, 44, 367
- Somerville, R. S., & Primack, J. R. 1999, *MNRAS*, 310, 1087
- Srianand, R., Hussain, T., Noterdaeme, P., et al. 2016, *MNRAS*, 460, 634
- Srianand, R., Noterdaeme, P., Ledoux, C., & Petitjean, P. 2008, *A&A*, 482, L39
- Steidel, C. C., Erb, D. K., Shapley, A. E., et al. 2010, *ApJ*, 717, 289
- Steidel, C. C., Strom, A. L., Pettini, M., et al. 2016, *ApJ*, 826, 159
- Steidel, C. C., Rudie, G. C., Strom, A. L., et al. 2014, *ApJ*, 795, 165
- Storey, P. J., & Zeppen, C. J. 2000, *MNRAS*, 312, 813
- Strom, A. L., Steidel, C. C., Rudie, G. C., et al. 2017, *ApJ*, 836, 164
- Sturm, E., González-Alfonso, E., Veilleux, S., et al. 2011, *ApJ*, 733, L16
- Sulentic, J. W., Marziani, P., & Dultzin-Hacyan, D. 2000, *ARA&A*, 38, 521
- Sun, A.-L., Greene, J. E., & Zakamska, N. L. 2017, *ApJ*, 835, 222
- Thomas, D., Maraston, C., Bender, R., & Mendes de Oliveira, C. 2005, *ApJ*, 621, 673
- Toft, S., Gallazzi, A., Zirm, A., et al. 2012, *ApJ*, 754, 3
- Trager, S. C., Faber, S. M., Worthey, G., & González, J. J. 2000, *AJ*, 119, 1645
- Trujillo, I., Förster Schreiber, N. M., Rudnick, G., et al. 2006, *ApJ*, 650, 18
- Turner, M. L., Schaye, J., Steidel, C. C., Rudie, G. C., & Strom, A. L. 2014, *MNRAS*, 445, 794
- , 2015, *MNRAS*, 450, 2067
- Tytler, D. 1987, *ApJ*, 321, 49
- van de Sande, J., Kriek, M., Franx, M., et al. 2013, *ApJ*, 771, 85
- van Dokkum, P. G., Kriek, M., & Franx, M. 2009, *Nature*, 460, 717
- van Dokkum, P. G., Franx, M., Kriek, M., et al. 2008, *ApJ*, 677, L5
- van Dokkum, P. G., Nelson, E. J., Franx, M., et al. 2015, *ApJ*, 813, 23
- Veilleux, S., & Osterbrock, D. E. 1987, *ApJS*, 63, 295
- Weatherley, S. J., Warren, S. J., Møller, P., et al. 2005, *MNRAS*, 358, 985
- Whitaker, K. E., van Dokkum, P. G., Brammer, G., & Franx, M. 2012, *ApJ*, 754, L29
- White, S. D. M., & Frenk, C. S. 1991, *ApJ*, 379, 52
- Wolfe, A. M., Gawiser, E., & Prochaska, J. X. 2005, *ARA&A*, 43, 861

- Worthey, G., Faber, S. M., & Gonzalez, J. J. 1992, *ApJ*, 398, 69
- Wuyts, E., Rigby, J. R., Sharon, K., & Gladders, M. D. 2012, *ApJ*, 755, 73
- Wuyts, S., Förster Schreiber, N. M., van der Wel, A., et al. 2011, *ApJ*, 742, 96
- York, D. G., Adelman, J., Anderson, Jr., J. E., et al. 2000, *AJ*, 120, 1579
- Yu, Q., & Tremaine, S. 2002, *MNRAS*, 335, 965
- Yuan, T.-T., & Kewley, L. J. 2009, *ApJ*, 699, L161
- Yuma, S., Ouchi, M., Drake, A. B., et al. 2017, *ArXiv e-prints*
- Zafar, T., Møller, P., Péroux, C., et al. 2017, *MNRAS*, 465, 1613
- Zafar, T., Popping, A., & Péroux, C. 2013, *A&A*, 556, A140